

Horizontal Distance of Each Cumulus and Cloud Broadening Distance Determine Cloud Cover

Yousuke Sato, Yoshiaki Miyamoto, Seiya Nishizawa, Hisashi Yashiro, Yoshiyuki Kajikawa,
Ryuji Yoshida, Tsuyoshi Yamaura, and Hirofumi Tomita
RIKEN Advanced Institute for Computational Science, Kobe, Hyogo, Japan

Abstract

We examine how cloud cover is determined in shallow-cloud areas by using large-eddy simulation with an extremely wide domain, which covers the transition phase from cumulus-understratocumulus to shallow-cumulus regimes. The relationship between two distances is critical to cloud cover. One characteristic distance is the horizontal distance between cumulus clouds, and the other is the broadening distance of anvil-like stratiform cloud at the top of the boundary layer. High cloud cover occurs with a long distance of broadening and short distances between cumuli. In contrast, low cloud cover appears with a short distance of broadening and a long distance between cumuli. The contrast of the two distances is rooted in aerosol amount and the strength of the surface heat flux. The relationship between these two distances can be applied to estimating the cloud cover below sharp inversions.

(Citation: Sato, Y., Y. Miyamoto, S. Nishizawa, H. Yashiro, Y. Kajikawa, R. Yoshida, T. Yamaura, and H. Tomita, 2015: Horizontal distance of each cumulus and cloud broadening distance determine cloud cover. *SOLA*, **11**, 75–79, doi:10.2151/sola.2015-019.)

1. Introduction

Clouds have a marked effect on the energy budget of the Earth (Trenberth et al. 2009). Among the several types of cloud, shallow clouds (e.g., stratus, stratocumulus, and shallow cumulus) play particularly important roles in the energy budget through radiation processes because they cover a broad area of the Earth (e.g., Randall et al. 1984). In climate prediction, the effects of clouds on the radiation budget are usually estimated through the radiative properties, for example, cloud optical thickness, effective radius, cloud fraction, cloud cover (e.g., Stephens 2005); therefore, shallow cloud cover is an important property that must be estimated correctly to improve climate prediction. Shallow clouds have been expressed by parameterizations in global-scale models (e.g., Tiedtke 1993; Considine et al. 1997). However, the parameterizations have not been able to simulate the shallow cloud cover observed from satellite (e.g., Chepfer et al. 2008; Naud et al. 2010); thus, it is necessary to improve understanding of the characteristics and parameterizations of shallow clouds to reduce uncertainties in climate prediction.

Shallow clouds are often generated off the west coast of continents under a sharp inversion of potential temperature (Klein and Hartmann 1993), and a transition from high cloud cover to low cloud cover often appears from the coast to the open ocean area. During the transition, solid stratus deck, cumulus under stratocumulus, and shallow cumulus are observed from the coast to the open ocean (Klein et al. 1995). High cloud cover occurs in the former two regimes, and cloud cover is low in the latter. The cloud cover below the sharp inversion changes drastically around the transition from cumulus under stratocumulus to shallow cumulus. In this paper, we target this phase to investigate the characteristics

of shallow cloud cover.

In the cumulus-under-stratocumulus regime, anvil-like stratiform clouds broaden horizontally at the top of the boundary layer (e.g., Kropfli et al. 1995). The wide broadening of the clouds enlarges the area of cloud coverage by stratiform cloud (Stevens et al. 2001). These results indicate that the extent of this broadening (lifetime of the stratiform cloud) is one of the key scales for cloud cover. Henceforth, we refer to this broadening as “cloud broadening,” and we refer to the distance of cloud broadening as “broadening distance.” In addition to cloud broadening from a single cumulus, the existence of multiple cumuli can affect the cloud cover. Cloud cover can be high when broadening clouds reach neighboring cumuli (Miller and Albrecht 1995). Cloud cover can also be high when individual cumuli are close to each other, even if the distance of cloud broadening is small. This suggests that the horizontal distance between cumuli is another key scale for cloud cover. Henceforth, we refer to this distance as “cumulus distance.”

To examine shallow cloud, many previous studies have used the large eddy simulation (LES) model (e.g., Bretherton et al. 1999; Stevens et al. 2001; Stevens et al. 2005; Xue et al. 2008; Ackerman et al. 2009; Sandu and Stevens 2011; Chung et al. 2012). However, their calculation domains were limited to several square kilometers due to a lack of computational resources. This domain size is too small to examine the effects of cloud broadening and multiple cumuli on cloud cover change because the horizontal distance of cloud broadening (i.e., several tens of kilometers; Wood 2012) is larger than the domain size. To investigate the relationship between these two distances and cloud cover, an experiment using an LES model with an extremely wide calculation domain covering several tens or hundreds of kilometers is required. The recent evolution of the supercomputer has facilitated such a large-scale simulation.

The purpose of this study was to (1) simulate the transition from cumulus under stratocumulus to shallow cumulus in the single-calculation domain, (2) investigate the relationship between the two distances, and (3) explore their contribution to determining shallow cloud cover.

2. Methodology

2.1 Model and experimental setup

The model used in this study was a fully compressible Large Eddy Simulation (LES) model in the Scalable Computing for Advanced Library and Environment library (SCALE-LES). The details of the LES model are described at <http://scale.aics.riken.jp/>. Subgrid-scale turbulence and microphysical processes were calculated using a Smagorinsky-type scheme (Scotti et al. 1993; Brown et al. 1994) and a two-moment bulk cloud microphysical scheme (Seiki and Nakajima 2014), respectively. We implemented a simple parameterization of radiative cooling based on an inter-comparison study of the Second DYNAMICS and CHEMISTRY OF MARINE STRATOCUMULUS (DYCOMS-II) first research flight (RF01) (Stevens et al. 2005), which was originally created from the δ -four stream radiative transfer model of Fu and Liou (1993).

The calculation domain in this study covered $768 \times 28 \times 2 \text{ km}^3$ with a horizontal grid interval (Δx and Δy) of 50 m and a vertical interval (Δz) of 5 m. An open boundary condition was imposed in the x direction, in the regions of $0 < x < 247 \text{ km}$ and $545 < x <$

768 km. The grid spacing in the x direction was stretched in these regions. In the z direction, a sponge layer was included in $z > 1200$ m in the same manner. In these regions, Rayleigh damping, which enforces the initial values, was applied for all prognostic variables to avoid artificial wave reflection. The damping coefficient increased linearly to the lateral boundary and model top. The damping time scale of horizontal and vertical direction was 300 and 10 s, respectively. These time scales were derived from sensitivity experiments (results not shown). The boundary condition in the y direction was periodic. The horizontally uniform initial profiles of potential temperature (θ), vapor mixing ratio (q_v), and liquid water mixing ratio (q_l) were the same as those in DYCOMS-II RF02 (Ackerman et al. 2009). For the wind profile, a uniform horizontal velocity of 5.0 m s^{-1} in the x direction was imposed in the whole calculation domain. The integration time was 16 h. We mainly discuss the snapshot of $t = 15.5$ h because the air mass located at $x = 247$ km (upwind lateral boundary) was carried to the downwind lateral boundary by the initial horizontal velocity at this time. The effects of spin-up are negligible around this time.

We configured the experiment so that the upwind region ($x = 0$ km) was a region of high cloud cover, as is often observed near the coastal area. In contrast, the downwind area ($x = 768$ km) mimicked a region of low cloud cover over the open ocean. To imitate an increase in sea surface temperature over the coastal region to the open-ocean region, surface latent heat (LH) flux, and surface sensible heat (SH) flux were increased from upstream to downstream as $LH(x) = 93 + 0.1365x \text{ W m}^{-2}$ and $SH(x) = 15 + 0.03062x \text{ W m}^{-2}$, respectively. These fluxes at $x = 0$ were the same as for DYCOMS-II RF02, which were derived from observations off the coast of California.

The number concentration of cloud condensation nuclei (CCN) (N_{ccn}) was a constant value during the simulation, $N_{ccn}(x) = 250 \exp(-7.0433 \times 10^{-3}x) \text{ cm}^{-3}$, in which the unit of x is km. This CCN setting imitates the decreasing trend of aerosol amount from the coastal area to the open ocean. The CCN number concentration at $x \sim 330$ km was 25 cm^{-3} , which was the threshold between high- and low cloud cover simulated by a previous study using SCALE-LES (Sato et al. 2014). A forcing of large-scale subsidence ($w_{LS} = Dz$) was given for all prognostic variables (ϕ) as $-\rho w_{LS} \frac{\partial \phi}{\partial z}$ based on Ackerman et al. (2009). The D was set to $1.33 \times 10^{-6} \text{ s}^{-1}$, the same as that used in Berner et al. (2011), ρ is total density whose unit is kg m^{-3} , and the unit of z is meters. We ignored the forcing of the Coriolis effect. The surface flux of momentum was the same as that in DYCOMS-II RF02. Random perturbations of θ (0.1 K) and q_v ($2.5 \times 10^{-6} \text{ kg kg}^{-1}$) were given below the boundary layer top (~ 795 m) at $t = 0$ to drive the turbulence. We expected that the above configurations of surface heat flux and CCN would simulate the transition from the cumulus-under-stratocumulus regime to the cumulus regime as in the observation.

2.2 Definition of the distance of cloud broadening and the cumulus distance

To analyze the distance of cloud broadening and the cumulus distance, we divided the whole calculation domain into nine regions, as shown in Fig. 1. We estimated these two distances in each region as follows. The distance of cloud broadening was estimated as the distance to which the anvil-like stratiform cloud extends from the convection center. The origin of the broadening distance was taken as the convection center because the stratiform

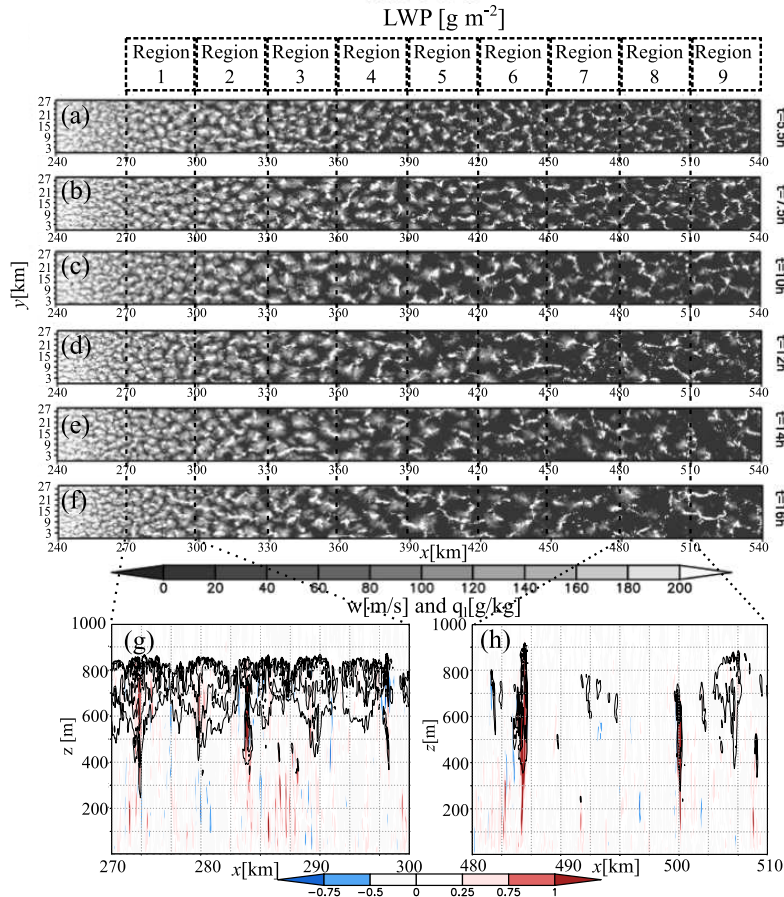


Fig. 1. Spatial distribution of the liquid water path at (a) $t = 5.5$ h, (b) $t = 7.5$ h, (c) $t = 10$ h, (d) $t = 12$ h, (e) $t = 14$ h, and (f) $t = 16$ h, and x-z slice of (contour) the liquid water mixing ratio ($q_l = q_c + q_v$) and (shaded) vertical velocity in (g) region 1 and (h) region 8 at $y = 15$ km at $t = 16$ h. The contour lines in (g) and (h) correspond to 0.25, 0.5, 0.75, and 1.0 g kg^{-1} , respectively.

clouds broaden horizontally around the top of each cumulus. The convection center was defined as the point at which the absolute value of vertical velocity (w) at $z = 500$ m and $t = 15.5$ h was larger than 3σ , in which σ is the standard deviation of w to the horizontally averaged w . Because several convection centers were extracted in each region, we created the mean radius–height distribution of q_l for each region. The ending point of cloud broadening was defined as the point at which q_l is smaller than the threshold value, $q_{l,t}$ ($= 2.2 \times 10^{-4}$ kg kg $^{-1}$). To calculate $q_{l,t}$, we assumed that the liquid water mixing ratio increased linearly with height (i.e., the cloud was adiabatic) and that the cloud geometrical thickness was 300 m, which was the initial geometrical thickness of clouds in the LES simulation.

The LES reproduced the transition from the closed cell structure in the cumulus-under-stratocumulus regime to the open cell structure in the shallow cumulus regime. The cumulus distance was determined as the distance between cells. The distance was estimated from the spectra of q_l averaged over 5 min around $t = 15.5$ h. We calculated the spectra at $z = 500, 600,$ and 700 m by the Fourier transformation. The cumulus distance was defined as the average of the wavelength of peak power among the three heights. The details of the methods are shown in Supplemental material.

3. Results and discussion

Figure 1 shows the temporal evolution of the liquid water path from $t = 5.5$ h to $t = 16$ h and an x - z slice of q_l and w in regions 1 (270 km $< x < 300$ km) and 8 (480 km $< x < 510$ km) at $y = 15$ km and $t = 16$ h. The contrast in cloud cover between the upwind and downwind regions becomes clear as the integration time increases. The cloud cover is high in the upwind regions (i.e., regions 1, 2, and 3), where a weak surface flux and large CCN concentration were given. In contrast, low cloud cover is apparent in the downwind regions (i.e., from regions 6 to 9), with strong surface flux and low CCN concentration. The x - z slice indicates that cumuli are generated in both the high- and low cloud cover areas. In the high cloud cover regions, stratiform cloud exists at the top of the boundary layer (Fig. 1g), whereas “shallow cumulus” dominates in the low cloud cover region (Fig. 1h). The cloud top height, which corresponds to the boundary layer top, in regions 1 and 8 is about 840 and 910 m, respectively. The difference in the cloud top height between high and low cloud cover regions is smaller than that observed in the *in situ* measurements. One of the reasons for the difference would be the horizontally uniform initial condition. An experiment using the initial condition, in which the top of the boundary layer gradually increases to the downwind region,

would reproduce a transition that is more realistic. However, we used horizontally uniform initial conditions to focus on the effects of CCN and surface heat flux in this study. We will conduct experiments using more realistic experimental setups in the future.

Figure 2 shows the vertical profiles of the total water mixing ratio ($q_t = q_l + q_r$), q_l , liquid water potential temperature (θ_l), precipitation flux, and third moment of grid resolved w' ($= w - \bar{w}$, in which \bar{w} is the horizontal average of w) averaged during $t = 15.5$ to 16 h. In the high cloud cover regions, both q_l and θ_l have a small vertical gradient below the top of the boundary layer. The precipitation flux at the surface is about 1 mm day $^{-1}$. The third moment of w' is positive, which indicates the existence of strong upward motion within a narrow area. These results indicate that cumulus-under-stratocumulus driven by the surface flux is successfully simulated. In the low cloud cover regions, the precipitation flux is larger than that in the high cloud cover region. Heavy precipitation removes liquid water from the atmosphere. Consequently, the peak value of q_l is small. The differences in q_l and θ_l between the ground and the top of the boundary layer are larger than those in the high cloud cover regions. It is worth simultaneously reproducing these aspects in a single calculation domain including the transition from the cumulus-under-stratocumulus regime to the shallow cumulus regime.

The horizontal wind field indicates that airmasses elevated by the updraft in the convection center diverge at the top of the boundary layer irrespective of the region (figure not shown). However, the distance of stratiform cloud broadening is wide only in the high cloud cover regions. The differences in the distance in each region can be interpreted as follows. In the low cloud cover regions, strong surface flux induces active convection and the low CCN concentration leads to fast conversion from cloud droplets to raindrops. Both effects contribute to generate strong precipitation. The strong precipitation removes liquid water from cumuli, and cloud broadening is confined to a narrow area. On the other hand, in the high cloud cover regions, convection is less active due to the weak surface flux. High CCN concentration suppresses the autoconversion process. They lead to weak precipitation and maintain liquid water in the cloud layer longer. Consequently, stratiform clouds tend to broaden more at the top of the boundary layer.

Figure 3 shows the distance of the cloud broadening, half of the cumulus distance, and cloud cover averaged over each region. The cumulus distance increases from the upwind region to the downwind region. The discontinuity of the distance from regions 5 to 6 occurs because the long-wavelength resolution is insufficient for resolving in the Fourier transform analysis. In contrast, the distance of the cloud broadening decreases from upwind to the downwind region. The distance in regions 1, 2, and 3 is not plotted. In

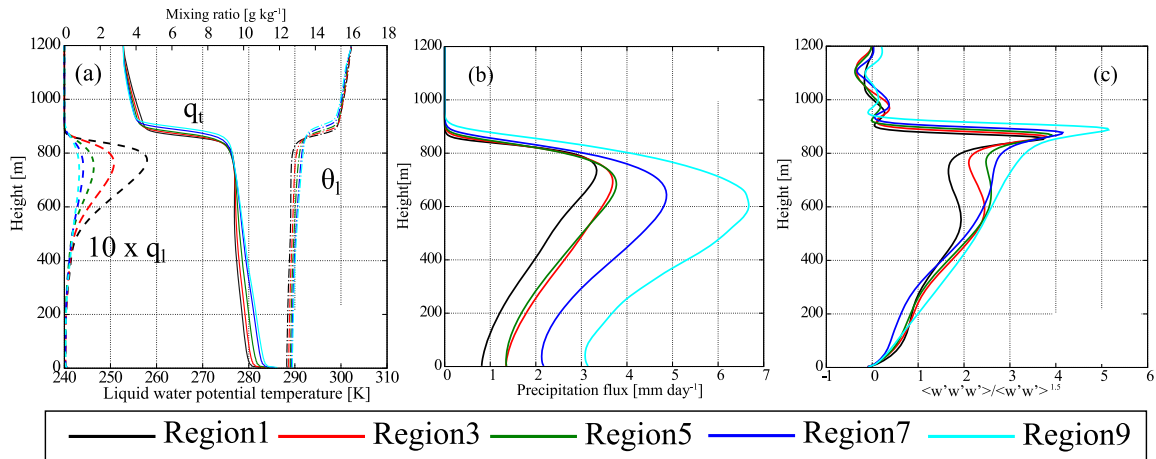


Fig. 2. Horizontally averaged vertical profile of (a) liquid water potential temperature (θ_l) (dot-dashed), total water mixing ratio ($q_t = q_c + q_r + q_v$) (solid), and tenfold liquid water mixing ratio (q_l) (dashed); (b) precipitation flux of cloudy columns, the liquid water path for which is larger than 20 g m $^{-2}$, and (c) third moment of w' normalized by w' variance to the power of 1.5 ($\langle w'w'w' \rangle / \langle w'w' \rangle^{1.5}$), averaged during the last 30 min (i.e., from $t = 15.5$ h to $t = 16$ h). To calculate the horizontally and temporally averaged vertical profile model outputs, data with 1-min intervals were used.

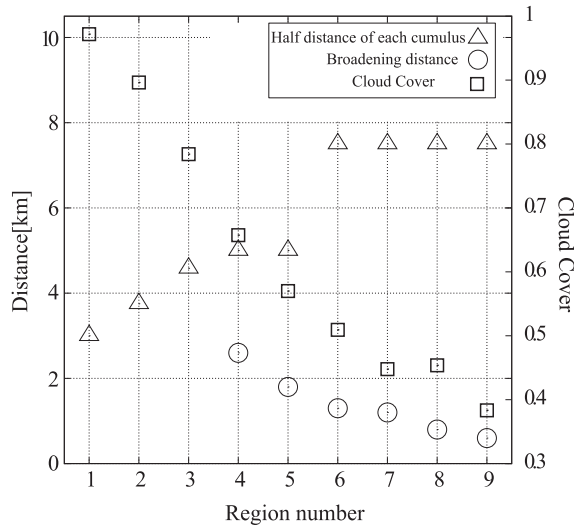


Fig. 3. The distance of cloud broadening (triangle), half-distance between cumuli (circle), and cloud cover (square) derived from the LES model result.

these regions, cloud broadens more widely than in other regions, and the distance of the cloud broadening is not explicitly determined because of the contamination of several clouds. However, analyses performed by using an ideal parcel model demonstrate that the distance of the cloud broadening increases on the order of region 3 < region 2 < region 1, and that the broadening distance exceeds or is comparable to half the cumulus distance in regions 1 and 2 (as shown in the supplemental material). Thus, the distance of the cloud broadening is longer than the cumulus distance in the upwind region, and vice versa in the downwind region.

In the upwind regions, the stratiform clouds broaden widely and the cumulus distance is short. In this case, the stratiform clouds can reach the stratiform clouds from neighboring cumuli before water droplets fall or are evaporated. Therefore, the cloud cover tends to be high (i.e., regional average of cloud cover is above 0.7). In the downwind regions, the cloud broadening distance is shorter than the cumulus distance. In this case, the stratiform cloud disappears until it extends to neighboring clouds. As a result, the cloud cover tends to be low (i.e., smaller than 0.5). Thus, the relationship between the distance of cloud broadening and the cumulus distance determines the cloud cover.

4. Concluding remarks and future work

We clarified that the relationship between the broadening distance of anvil-like stratiform clouds and the horizontal distance between cumuli determines shallow cloud cover. We clarified this by using a high-resolution LES model with an extremely wide domain. These two distances are important for determining shallow cloud cover in the transition phase from cumulus under stratocumulus to shallow cumulus. Figure 4 is a conceptual illustration of our interpretation of the relationship between cloud cover and the two distances. In the cumulus-under-stratocumulus regime, the distance between cumuli is smaller than the broadening distance of stratiform clouds at the top of the boundary layer. Each stratiform cloud can extend to its neighboring clouds. High cloud cover over 0.7 appears in this case (Fig. 4a). In the shallow-cumulus regime, a cloud cannot extend to the next cloud for two reasons: (1) the long distance between cumuli, and (2) the small extent of cloud broadening. In this case, cloud cover is low (Fig. 4b). Thus, the relationship between the distance between cumuli and the broadening distance of the stratiform clouds determines the shallow cloud cover.

Long (short) broadening distance of the anvil-like stratiform clouds occurs with weak (strong) surface heat flux and large (small)

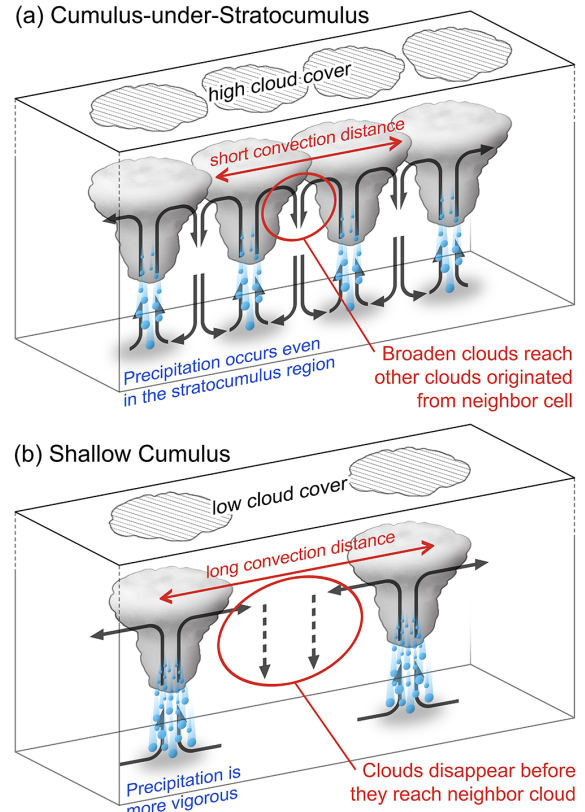


Fig. 4. Schematic illustration of an overhead and a side view of (a) the high cloud cover (cumulus-under-stratocumulus) region and (b) the low cloud cover (shallow-cumulus) region.

amounts of aerosol. In contrast, long (short) distance between cumuli appears when the surface heat flux and aerosol amounts are strong and small (weak and large), respectively. We can apply the relationship between the two distances to estimate shallow cloud cover in global-scale models with coarse grid resolution. This result contributes to improvement of the parameterizations of shallow clouds and to reduction of the uncertainties of climate prediction caused by shallow clouds. For actual improvement of shallow cloud parameterization, it is a key to incorporate the dependency of cloud cover to the cloud broadening distance and distance between cumuli into the parameterization scheme. We will attempt to incorporate it in the near future.

In this study, the contrast of these distances between high- and low cloud cover regions was generated by the differences of CCN and surface flux. Sensitivity experiments with separately changing CCN concentrations and surface heat flux are required to quantitatively evaluate the contribution of each factor.

In addition to the sensitivity experiment, an experiment covering a large calculation domain for both the x and y directions is also required, because the cumulus distance in the downwind region (e.g., regions 8 and 9) would be limited by the domain size in the y direction. To make our suggestion more robust, we will conduct these experiments in the near future.

Acknowledgements

Part of the results is obtained by the K computer at the RIKEN Advanced Institute for Computational Science. (AICS team resource, and resource from proposal number hp140046). Figure 1 was created by Grid Analysis and Display System (GrADS). Figures 2 and 3 were created by the Gnuplot. The authors would like to thank to S. A. Adachi, our colleagues, and anonymous reviewers for fruitful discussions.

Supplement

Supplement 1 indicates the sensitivity experiment of aerosol amount to the cloud broadening distances using a parcel model. Supplement 2 describes the method to estimate the distance of cloud broadening and cumulus distance.

References

- Ackerman, A. S., and co-authors, 2009: Large-eddy simulations of a drizzling, stratocumulus-topped marine boundary layer. *Mon. Wea. Rev.*, **137**, 1083–1110, doi:10.1175/2008MWR2582.1.
- Berner, A. H., C. S. Bretherton, and R. Wood, 2011: Large-eddy simulation of mesoscale dynamics and entrainment around a pocket of open cells observed in VOCALS-REx RF06. *Atmos. Chem. Phys.*, **11**, 10525–10540.
- Bretherton, C. S., S. K. Krueger, M. C. Wyant, P. Bechtold, E. Van Meijgaard, B. Stevens, and J. Teixeira, 1999: A GCSS boundary-layer cloud model intercomparison study of the first ASTEX lagrangian experiment. *Boundary-Layer Meteorol.*, **93**, 341–380.
- Brown, A. R., S. H. Derbyshire, and P. J. Mason, 1994: Large-eddy simulation of stable atmospheric boundary layers with a revised stochastic subgrid model. *Q. J. R. Meteor. Soc.*, **120**, 1485–1512.
- Chepfer, H., S. Bony, D. Winker, M. Chiriaco, J. L. Dufresne, and G. Sèze, 2008: Use of CALIPSO lidar observations to evaluate the cloudiness simulated by a climate model. *Geophys. Res. Lett.*, **35**, 1–6, doi:10.1029/2008GL034207.
- Chung, D., G. Matheou, and J. Teixeira, 2012: Steady-state large-eddy simulations to study the stratocumulus to shallow-cumulus cloud transition. *J. Atmos. Sci.*, **69**, 3264–3276, doi:10.1175/JAS-D-11-0256.1.
- Considine, G., J. A. Curry, and B. Wielicki, 1997: Modeling cloud fraction and horizontal variability in marine boundary layer clouds. *J. Geophys. Res.*, **102**, 13517–13525, doi:10.1029/97JD00261.
- Fu, Q., and K. N. Liou, 1993: Parameterization of the radiative properties of cirrus clouds. *J. Atmos. Sci.*, **50**, 2008–2025.
- Klein, S. A., and D. L. Hartmann, 1993: The seasonal cycle of low stratiform clouds. *J. Clim.*, **6**, 1587–1606.
- Klein, S. A., D. L. Hartmann, and J. R. Norris, 1995: On the relationships among low-cloud structure, sea surface temperature, and atmospheric circulation in the summertime northeast Pacific. *J. Clim.*, **8**, 1140–1155.
- Kropfli, R. A., and co-authors, 1995: Cloud physics studies with 8 mm wavelength radar. *Atmos. Res.*, **35**, 299–313.
- Miller, M. A., and B. A. Albrecht, 1995: Surface-based observations of mesoscale cumulus–stratocumulus interaction during ASTEX. *J. Atmos. Sci.*, **52**, 2809–2826.
- Naud, C. M., A. D. Del Genio, M. Bauer, and W. Kovari, 2010: Cloud vertical distribution across warm and cold fronts in cloudsat-CALIPSO data and a general circulation model. *J. Clim.*, **23**, 3397–3415.
- Randall, D. A., J. A. Coakley, D. H. Lenschow, C. W. Fairall, and R. A. Kropfli, 1984: Outlook for research on subtropical marine stratification clouds. *Bull. Amer. Meteor. Soc.*, **65**, 1290–1301.
- Sandu, I., and B. Stevens, 2011: On the factors modulating the stratocumulus to cumulus transitions. *J. Atmos. Sci.*, **68**, 1865–1881, doi:10.1175/2011JAS3614.1.
- Sato, Y., S. Nishizawa, H. Yashiro, Y. Miyamoto, and H. Tomita, 2014: Potential of retrieving shallow-cloud life cycle from future generation satellite observations through cloud evolution diagrams: a suggestion from a large eddy simulation. *SOLA*, **10**, 10–14.
- Scotti, A., C. Meneveau, and D. K. Lilly, 1993: Generalized smagorinsky model for anisotropic grids. *Phys. Fluids A Fluid Dyn.*, **5**, 2306–2308.
- Seiki, T., and T. Nakajima, 2014: Aerosol effects of the condensation process on a convective cloud simulation. *J. Atmos. Sci.*, **71**, 833–853.
- Stephens, G. L., 2005: Cloud feedbacks in the climate system: a critical review. *J. Clim.*, **18**, 237–273.
- Stevens, B., and co-authors, 2001: Simulations of trade wind cumuli under a strong inversion. *J. Atmos. Sci.*, **58**, 1870–1891.
- Stevens, B., and co-authors, 2005: Evaluation of large-eddy simulations via observations of nocturnal marine stratocumulus. *Mon. Wea. Rev.*, **133**, 1443–1462.
- Tiedtke, M., 1993: Representation of clouds in large-scale models. *Mon. Wea. Rev.*, **121**, 3040–3061.
- Trenberth, K. E., J. T. Fasullo, and J. Kiehl, 2009: Earth’s global energy budget. *Bull. Amer. Meteor. Soc.*, **90**, 311–323.
- Wood, R., 2012: Stratocumulus clouds. *Mon. Wea. Rev.*, **140**, 2373–2423.
- Xue, H., G. Feingold, and B. Stevens, 2008: Aerosol effects on clouds, precipitation, and the organization of shallow cumulus convection. *J. Atmos. Sci.*, **65**, 392–406.

Manuscript received 10 March 2015, accepted 9 May 2015
 SOLA: <https://www.jstage.jst.go.jp/browse/sola/>